IEEE Access
Multidisciplinary | Rapid Review | Open Access Journal

Received January 29, 2019, accepted February 20, 2019, date of publication March 11, 2019, date of current version March 26, 2019.

Digital Object Identifier 10.1109/ACCESS.2019.2903467

Bandlets on Oriented Graphs: Application to Medical Image Enhancement

RAHELE KAFIEH[1], (Member, IEEE), HOSSEIN RABBANI[1], (Senior Member, IEEE), AND GOZDE UNAL[2], (Senior Member, IEEE)

[1]Medical Image and Signal Processing Research Center, Department of Biomedical Engineering, Isfahan University of Medical Sciences, Isfahan 81746-73461, Iran

[2]Department of Computer Engineering, Istanbul Technical University, 34469 Istanbul, Turkey

Corresponding author: Gozde Unal (unalgo@itu.edu.tr; gozde.unal@gmail.com)

This work was supported in part by the TUBITAK 2216 Research Fellowship Program.

ABSTRACT In this paper, we introduce a new image modeling method by getting benefit from both sparsity and multiscale characteristics of transform-domain modeling, along with the geometrical representation of the graph-based models. The proposed method is named bandlet on an oriented graph (BOG) and improves directional selectivity property of the bandlets. The conventional wavelet in the bandlet design is substituted with a new non-orthogonal wavelet. The replaced wavelet is defined on a graph. In order to adjust the orientation of the wavelet atoms with the corresponding edges in the image pixels, a directed graph is constructed. The resultant wavelets in discrete scales can be considered as a frame and are created to build a tight frame. To show the effectiveness of this new atomic representation, we demonstrated the performance of the new model in noise alleviation of the optical coherence tomography (OCT) images (from the retina) and microscopic images. Denoising results on OCT are reported on 72 slices, selected arbitrarily out of OCT dataset from Topcon device. The combined method provided an enhancement of contrast to noise ratio (CNR) (from 27.82 to 30.11), and improvement of the equivalent number of looks (ENL) (from 2183.26 to 2217.37) over the state-of-the-art in OCT noise reduction. In the denoising of microscopic images, PSNR improvement (from 26.33 to 35.24) over the original image is shown along with the improvement in next steps of feature extraction.

INDEX TERMS Image modeling, multiscale graph analysis, bandlets, oriented graphs, wavelets, image denoising, bandlets on oriented graphs.

I. INTRODUCTION

Image modeling which aims at describing properties of images in general can be considered as one of the most crucial steps for a majority of image analysis tasks such as image filtering, segmentation, coding, classification, registration and so on. As the model becomes more appropriate for a signal, the corresponding analysis becomes more powerful. Prevalent image modeling methods can be categorized according to the image domain: spatial and transform domain [1]. Depending on the modeling point of view, both models in spacial and transform domain may be devised as deterministic, random, geometrical, or PDE oriented models. Different transform domain models (like single scale Fourier transform, multiscale X-lets [2]–[6], and data adaptive models like Independent Component Analysis (ICA) [7], Principle Component Analysis (PCA) [8] and Dictionary Learning (DL) methods [9]) are already well-known in image processing [1]. However, combination of the transform domain techniques with geometric modeling is quite recent in the literature. Extension of the corresponding transform from regular domains to irregular, non-Euclidean spaces like a sphere [10], other conic sections [11], or vertices of a weighted graph are examples of such compositions. Graphs can represent many datasets like computer networks, transportation networks or social networks. They have become common recently in image modeling for different applications like segmentation, clustering, and filtering [12], [13].

The combination of transform domain techniques with graph modeling goes back to wavelets on un-weighted graphs, which is introduced for analysis of computer networks [14], [15]. Another approach is a generic theory to

The associate editor coordinating the review of this manuscript and approving it for publication was Sun-Yuan Hsieh.

decompose the wavelets using tight interpretation of a diffusion operator with different powers [16]. A different kind of wavelets is developed over compact manifolds is in [17] and graph wavelet transform in spectral domain is introduced by Hammond *et al.* [18]. A more recent work suggests application of dictionary learning methods to represent graph signals sparsely [19]. Taking advantage of both sparsity and multiscale characteristics of transform domain modeling, along with geometrical representation of graph based models, these combined methods are more powerful compared with their original counterparts. In this paper, inspired by those developments, we introduce a new blend of the mentioned transform domain modeling strategies to achieve our goal of image denoising.

Extensions of wavelet transform, which is the most popular transform domain approach, to higher dimensional spaces (like images and volumes) are first introduced based on products of one dimensional wavelets [20]. However, an undesirable bias for fixed wavelet directions, yields to introduction of geometrical X-lets including Laplacian pyramids [21], dual-tree wavelets [22], curvelet transfroms [23], and bandlet transforms [24].

Wavelet based processing performs well on natural images but it is not optimal in approximation of geometrically regular images. The reason is that isotropic support of wavelets misses the regularity of the edges in arcs. To overcome this problem, a bandlet approximation is introduced in [24]. Bandlet transform [24]–[26] captures the redundancy in wavelet coefficients by means of another transformation on multiscale coefficients. For example, in a denoising application, the bandletization demands no statistical model and using individual thresholding on resulted coefficients results in an optimum estimate in the sense of the average quadratic risk for geometric images. A bandlet basis is constructed upon a wrapped version of a wavelet basis along the flow of image gradients, with emphasis on regularity of the image along the geometric flow. This version was non orthogonal and suffered from boundary artifacts due to warping. In the second generation of bandlets [27], these issues were solved by reordered version of 2D wavelet coefficients, followed by a 1D wavelet transform. The bandlet transform in image denoising is proven to surpass the performance of translation invariant wavelet frames [28] and the methods that use advanced statistical modeling for the wavelet coefficients (BLS-GSM [29]). The recovered edges are more sharp and less vibrating results are observed in bandlet results [25]. However, dependency of the bandlet transform on the wavelet coefficients remains as a constraint.

In this paper, to overcome the above constraint and improve the directionality properties of the bandlets, we propose a new wavelet to replace the conventional wavelet in the bandlet design. The new wavelet is defined on a directed graph and its atoms are trained to be oriented according to the edges in an image. We call the new method as the bandlet on an oriented graph (BOG) and demonstrate its ability in noise reduction of the retinal images.

II. BACKGROUND

A. SPACE-FREQUENCY ANALYSIS ON A GRAPH

In order to define the wavelet transform on graphs, one should overcome the complication of scaling on discrete graph nodes. Although several solutions are proposed for this problem, we adopt the recent method by Hammond *et al.* [18] who introduced a new approach using spectral theory as follows.

On a constant scale s, the wavelet transform can be defined as a transform on function f:

$$\left(T^s f\right)(x) = \frac{1}{2\pi}\int_{-\infty}^{\infty} e^{i\omega x}\hat{\psi}^*(s\omega)\hat{f}(\omega)\,d\omega \tag{1}$$

where $\hat{f}(.)$ denotes the Fourier transform upon function f, $\hat{\psi}^*(.)$ denotes the Fourier transform opun wavelet function $\psi(.)$, i stands for square root of -1, and ω is the angular frequency. Note that the scale s is only available in $\hat{\psi}^*(s\omega)$, which transfers the scale parameter to the Fourier domain.

With selection of a kernel $g : \mathbb{R} \to \mathbb{R}^+$, it is possible to define the wavelet transform. g should be a band pass filter: $g(0) = 0$, and $\lim_{x\to\infty} g(x) = 0$. Then, the wavelet operator $T_g = g(\mathcal{L})$ defined on the Laplacian graph $\mathcal{L}$ that uses the eigenvectors and the eigenvalues of the Laplacian operator, χ_l and λ_l, $\ell = 0, 1 \ldots, \mathrm{N}-1$ where N represents the number of nodes of the graph, may be applied on the function f:

$$W_f(t,n) = (T_g^t f)(n) = \sum_{\ell=0}^{N-1} g(t\lambda_\ell)\hat{f}(\ell)\chi_\ell(n). \tag{2}$$

where t is scale of the wavelet operator and n is the vertex number and $\hat{f}(\ell)$ denotes the $\hat{f}(.)$ (Fourier transform) on the ℓth node.

In this structure, the spectral graph wavelets are orthogonal to χ_0 and nearly orthogonal to any χ_ℓ whose corresponding λ_1 is near to zero. Similar to conventional wavelets, for representation of low-frequency contents of f, another class of functions (scaling functions) is required. With selection of a kernel $h : \mathbb{R} \to \mathbb{R}^+$, as a lowpass filter, $h(0) > 0$, and $h(x) \to 0$ if $x \to 0$, scaling functions are defined as $\phi_n = T_h\delta_n = h(\mathcal{L})\delta_n$ and the coefficients are obtained by $S_f(n) = \langle\phi_n, f\rangle$, where δ_n is the Dirac delta function at vertex n.

Reconstruction can be obtained from:

$$\frac{1}{C_g}\sum_{n=1}^{N}\int_0^{\infty} W_f(t,n)\psi_{t,n}(m)\frac{dt}{t} = f^{\#}(m) \tag{3}$$

where C_g is a constant depending on kernel g. Then we have:

$$f = f^{\#} + \hat{f}(0)\chi_0. \tag{4}$$

However, the reconstruction is more complicated in real implementation and for more details we refer the reader to [18].

Since in an implementation of the given method, the scaling values of t become discrete, the above equation is only valid theoretically. Instead, limited number of scales (J) are selected and t values are quantized by $\{t_j\}_{j=1}^{J}$. Namely, the number of wavelets $\psi_{t_j,n}$ are NJ and the number of scaling functions ϕ_n are N. In order to understand how well

these vectors represent functions defined on graph nodes, the wavelets in discrete scales can be considered as a frame and boundaries of the frame can be studied. It is well-known that in Hilbert space H, vectors $\Gamma_k \in \mathcal{H}$ make a frame with boundaries A and B, if:

$$A \|f\|^2 \leq \sum_k |\langle f, \Gamma_k \rangle|^2 \leq B \|f\|^2 \tag{5}$$

is correct for all $f \in \mathcal{H}$. Those boundaries give information about the stability of the reconstruction of f using $\langle f, \Gamma_k \rangle$ coefficients which are $W_f(t, n)$ and $S_f(n)$ in this case. It can be shown that:

$$A = min_{\lambda \in [0, \lambda_{N-1}]} G(\lambda) \tag{6}$$

$$B = max_{\lambda \in [0, \lambda_{N-1}]} G(\lambda) \tag{7}$$

where $G(\lambda) = h(\lambda)^2 + \sum_{j=1}^{J} g(t_j \lambda)^2$ as given by Hammond *et al.* [18].

B. ORIENTED WAVELET ON GRAPH

As oriented structures like edges are abundant in images, oriented wavelets are naturally more appropriate tools in image processing compared to isotropic filters [30]. Therefore, a considerable size of previous literature is devoted to obtain well-oriented wavelets [31].

In a simple construction of the graph, the equal weights of connections to 8 neighbors produce isotropic wavelets, not a sparse basis for representation of images. However, a wise selection of the weights can lead to oriented wavelets. For this purpose, the Laplacian of the graph should approximate a second-order derivative operator [31]. Using two parameters of θ (for orientation) and $\delta \in [0, 1]$ (for level of orientedness), for each θ, the second-order derivative operator with a full-level orientation is given by:

$$\left(D_\theta^2 f\right)(x, y) = \frac{d^2}{d\varepsilon^2} f\,(x + \varepsilon cos\theta, y + \varepsilon sin\theta)|_{\varepsilon=0}\,. \tag{8}$$

For $\delta < 1$, the operator $D(\varepsilon, \theta)$ contains a portion of the second-order derivative value in the perpendicular direction:

$$D(\delta, \theta) = \frac{1+\delta}{2} D_\theta^2 + \frac{1-\delta}{2} D_{\theta+\frac{\pi}{2}}^2\,. \tag{9}$$

It can be also shown that [32]:

$$D(\delta, \theta) = \frac{1}{2}(1 + \delta cos2\theta) f_{xx} + (\delta sin2\theta) f_{xy} + \frac{1}{2}(1 - \delta cos2\theta) f_{yy}. \tag{10}$$

The connectivity values to 8 neighbors are then defined by $W_{\delta,\theta}^{loc}$ as $d_1, d_2, \ldots, d_8$ as depicted in Figure 1. For the sake of symmetry of the wavelets, the weights should be symmetric, which requires calculation of only 4 d values, hence leads to a 4 dimensional $d \in \mathbb{R}^4$ (dNW = dSE, dN = dS, dNE = dSW, dE = dW).

Let f be a continuous function sampled on nodes of a graph, and let f_i be the values of f on 8 neighbors in Figure 1. x_i and y_i are integer offsets for node i, for instance

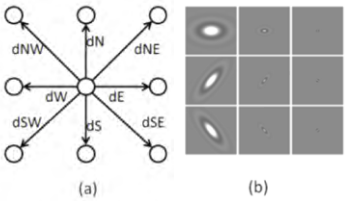

FIGURE 1. (a) Eight neighbors connections, (b) Sample wavelets [31]. N, S, E, and W stand for North, South, East, and West.

$(x_1, y_1) = (-1, 1)$. Assuming that distance between the nodes is Δ, a second order Taylor expansion yields to:

$$f_i - f_0 = \Delta\left(x_i f_x + y_i f_y\right) + \frac{1}{2}\Delta^2 \times \left(x_i^2 f_{xx} + 2x_i y_i f_{xy} + y_i^2 f_{yy}\right) + o(\Delta^3) \tag{11}$$

where f_0 represents the central node of the graph. By applying Laplacian on f in the central node, we get:

$$\sum_i d_i (f_i - f_0) = \Delta^2 \left(f_{xx} \sum_i \frac{1}{2} d_i x_i^2 + f_{xy} \sum_i d_i x_i y_i + f_{yy} \sum_i d_i y_i^2\right) + o\left(\Delta^3\right) \tag{12}$$

Assuming $\Delta = 1$, and equating values of f_{xx}, f_{yy}, and f_{xy} in 10 and 12:

$$\begin{cases} d_1 + d_3 + d_4 = \frac{1}{2}(1 + \delta cos2\theta) \\ -d_1 + d_3 = \frac{1}{2}\delta sin2\theta \\ d_1 + d_2 + d_3 = \frac{1}{2}(1 - \delta cos2\theta) \end{cases} \Leftrightarrow Md = v(\theta, \delta) \tag{13}$$

where

$$M = \begin{pmatrix} 1 & 0 & 1 & 1 \\ -1 & 0 & 1 & 0 \\ 1 & 1 & 1 & 0 \end{pmatrix}, v = \left(\frac{1}{2}, 0, \frac{1}{2}\right)^T + \frac{\delta}{2}\left(cos\frac{\theta}{2}, sin\frac{\theta}{2}, -\cos\frac{\theta}{2}\right)^T.$$

Since the graph weights should be positive, the final relation to be solved is given by:

$$d^*(\theta, \delta) = argmin_d \|d\|^2 \quad subject\ to\ Md = v(\theta, \delta),\ and\ d_i \geq 0 \tag{14}$$

This equation is solved for a given set of θ directions, and $\delta \approx 0.44$ as in [31].

C. SECOND GENERATION BANDLET TRANSFORM

Second generation bandlet transform is proposed on a standard orthogonal wavelet transform, first by changing the order of 2D wavelet coefficients (Figure 2, b) and next by applying a 1D wavelet transform [27]. Bandletization wipes away the available correlation among wavelet coefficients located close to singular regions. To skim off the mentioned

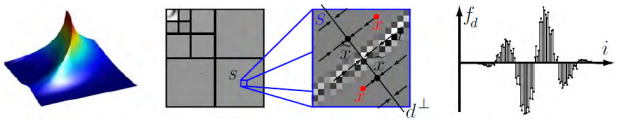

FIGURE 2. Steps of original bandlet transform [27].

redundancy, regularities in the wavelet transform of the surface should be detected to construct a tailored approximation.

Two main steps can be defined for bandletization. In first step, the points should be reordered. For this purpose, we select a square S with width of L at some scale $2^j$and orientation $s \in \{H, V, D\}$ in wavelet domain (figure 2, c). The main purpose is to remove the non isotropic redundancy which cannot be wiped out using 2D wavelet transform. For this purpose, the wavelet points are ordered again to provide a smooth 1D discrete signal (Figure 2, d). In order to retrieve the geometrical regularity near sharp points, directional projections by reordering along a parallel to the real geometry can be achieved [27].

In step 2 of bandletization, a one dimensional wavelet transform is incorporated on the one dimensional discrete signal. This transform can also discriminate between good and bad reordering. Bandlet coefficients below a selected T will be dumped, and higher T leads to a more aggressive compression. The goal is finding a new order, or the size of square S with a selected direction d, which yields to less posssibleone dimensional coefficients more than the selected T. Method: Bandlet on Oriented Graphs

According to the conventional bandlet theory [27], bandletization removes the redundancy in the 2D wavelet transform due to regularity caused by wavelets and further regularity along the geometry. When using the conventional 2D wavelet transform, three mother wavelets $\{\psi^H, \psi^V, \psi^D\}$ (horizontal, vertical and diagonal) are responsible for this geometry. However, if the number of wavelet directions would increase, more regularity and correspondingly, more effective bandletization can be expected. Wavelet on the graph has the intrinsic characteristic to produce wavelets in every single direction. Furthermore, the rotated wavelets are regular and without checkerboard artifact which can also increase the needed regularity. Although the wavelet on the graph can theoretically produce any wavelet rotation direction, we have to select a limited number of rotation values due to complexity considerations. The development below and results are reported on 8 directions.

When substituting the conventional wavelet with the wavelet on the graph, the first question is how to set the correct direction for wavelets. Namely, if we use the conventional wavelet on the graph, one single set of (θ, δ) can be selected for each image (let's say a given θ_0 and $\delta_0 \approx 0.44$). The weights of connections to 8 neighbors should be calculated from Eq.14, for this set. The resulting vector $d = (d_1, d_2, d_3, d_4)$ will constitute the weights of the graph and all the nodes have the same connection weights. A sample

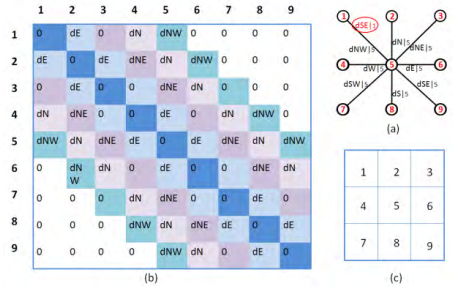

FIGURE 3. a) graph weights, (b) similarity matrix, (c) numbering of a 3 × 3 image pixels for construction of a 8 neighbors graph.

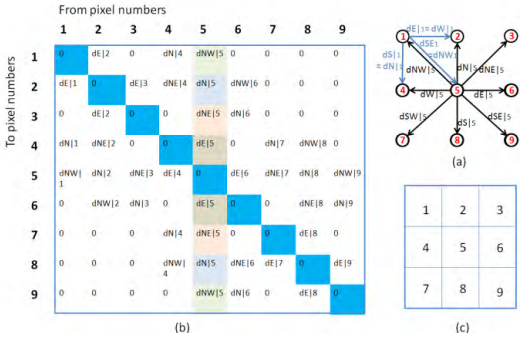

FIGURE 4. a) weights of a directed graph, (b) similarity matrix, (c) numbering of a 3 × 3 image pixels for construction of a 8 neighbors graph.

similarity matrix for a 3 × 3 image is shown in Figure 3. The resulting wavelet coefficients will produce a 2D wavelet output which concentrates on edges in θ_0 direction.

In the proposed method, in order to consider different orientations, let us estimate the orientation of each pixel and calculate corresponding d values from Eq.14. The weights of the graph connections, starting from that pixel to the neighboring pixels is set to these d values. For example, pixel 5 in Figure 3 is considered with orientation equal to θ_5. The corresponding d values are $d|_5 = (\text{dNW}|_5, \text{dN}|_5, \text{dNE}|_5, \text{dE}|_5)$. However, a problem with non oriented graphs arises here, which is for a neighbor-ing pixel like 1, the orientation θ_1 is not essentially equal to θ_5 and corresponding $d|_1 = (\text{dNW}|_1, \text{dN}|_1, \text{dNE}|_1, \text{dE}|_1)$ will enforce other set of weights to the connecting edge. In this case, the weight of the connection between pixel 5 and 1 will be determined with two different values $\text{dNW}|_5$ and $\text{dNW}|_1 = \text{dSE}|_1$ (See Fig. 3.a).

D. CONSTRUCTION OF A DIRECTED GRAPH

To solve the problem described above, we propose a directed graph as shown in Figure 4. The weights from one node are then calculated according to orientation of the source node (second index). It means that the Eq.14 is solved for each orientation θ; furthermore, δ value is set to 0.44 except if the pixel is identified to be located in a smooth patch. In the latter case, δ is set to 1, which yields an isotropic wavelet instead of anisotropic cases.

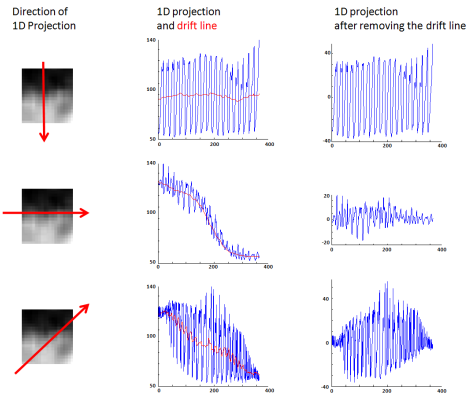

FIGURE 5. Proposed method to calculate orientation of each pixel. Left column) A window of size 20 × 20 is selected around each pixel, Middle column) 1D projection of the pixel values are obtained in 8 selected directions, Right column) the drift line of the 1D projection is removed.

With this new construction, the symmetry of weights for each node is preserved, but the resulting matrix is nonsymmetrical because of the intrinsic properties of the directed graph.

E. CALCULATION OF ORIENTATION

In order to calculate the orientation of each pixel, we present a simple yet intuitive strategy. A window of size N×N (e.g. 20 × 20) is selected around each pixel and a 1D projection of the pixel values are obtained in 8 selected directions. The drift line of the 1D projection is then removed and the sum of absolute values for deviations from zero line is obtained. The direction with the smallest sum is then accepted as the correct orientation. This method is depicted in Figure 5. Furthermore, according to a user-defined threshold value, the pixel whose sum value is less than the threshold is identified to be located in a smooth patch.

F. CALCULATION OF EIGENVALUES AND EIGENVECTORS

In the proposed BOG method, in order to design the wavelet transform on a directed graph, the main problem one should solve is the calculation of eigenvectors/values in a nonsymmetrical matrix. It is possible to design a numerical method for symmetric matrices. However, due to inherent characteristics of non-symmetric matrices such as very sensitive eigenvalues to little alternations of the matrix elements, calculations for this category are not straightforward [32].

As a solution, we start with a reduction of the matrix to a simpler form, e.g. the Hessenberg form, to prepare it for further iterative procedures of eigenvalue/vector computations. The upper Hessenberg matrix has elements equal to zero in locations beneath the diagonal except the elements located in first diagonal line. It should be emphasized that the matrix constructed in our method from the non symmetric graph is originally very near to a Hessenberg form because its intrinsic properties (by construction) lead most of the below-diagonals to zero and correspondingly make the calculation of an upper Hessenberg matrix easier.

Two main approaches are used to change a matrix to an upper Hessenberg form. The first scheme is applying a series of Householder transformations, to zero needed elements in specified columns of the matrix. The second and more efficient method is Gaussian elimination with pivoting.

Employing the method based on Gaussian elimination, we call the matrix before the rth stage A_r, and the original matrix $A = [a_{jk}] = A_1$. Now, A_r becomes upper Hessenberg for first $r-1$ columns and rows. The rth step is then like:

1- Search in the rth column below the diagonal to find the element with maximum magnitude. If it is "zero", the stage is done. Go to the next stage. Otherwise, the maximum value is in row r'.

2- Change the values in row r' and $r+1$ (Pivoting procedure). Do the same for column r' and $r+1$.

3- For $i = r+2, r+3, \ldots, N$, compute:

$$n_{i,r+1} = a_{ir}/a_{r+1,r}. \tag{15}$$

Subtract $n_{i,r+1}$ times row $r+1$ from row i. Also add $n_{i,r+1}$ times column i to column $r+1$ [32], [33].

After calculation of an upper Hessenberg matrix, an improved QR algorithm with spectral shifts can be used to calculate the eigenvectors [34]. Let λ be an eigenvalue of the Hessenberg matrix H. We consider:

$$1 : H - \lambda I = QR \ (QR \text{ factorization }) \tag{16}$$

$$2 : \bar{H} = RQ + \lambda I \tag{17}$$

It can be shown that $H \sim \bar{H}$ but $\bar{H}$ is a smaller matrix with easier calculations. However, since we don't have access to λ, a Rayleigh quotient shift can estimate the value to be equal to the last diagonal element of the Hessenberg matrix. This substitution of $\bar{H}$ in QR decomposition is named shifted QR method [34], which is used in our work to calculate the eigenvalues.

G. FILTER DESIGN

The next stage in the BOG method is to design effective scaling kernels and wavelet kernels. It can be proved that a band pass and monic g filter like the one defined by Hammond *et al.* [18] leads to an acceptable wavelet on the graph. Remembering that scaling kernels are selected independently from wavelet kernels (with the only limiting criteria on value of $G(\lambda)$), Hammond *et al.* [18] also proposed a function for h.

However, as in this work, our focus is on the denoising application, a stable reconstruction becomes more important. Therefore, design of kernels leading to a tight frame is an ideal replacement for conventional kernels. In such frames, values of frame boundaries (A and B in (5)) are equal and the re-construction is improved in terms of speed and accuracy [35].

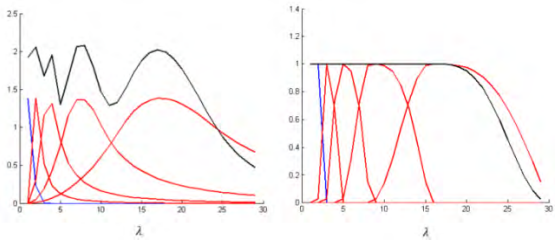

FIGURE 6. Sample of kernels for construction of the scaling function $h(\lambda)$ in blue, the wavelet functions $g(t_j\lambda)$ in red, and $G(\lambda)$ in black using conventional kernel values by Hammond *et al.* [18] (left) and Held kernels [36] used in our proposed method (right).

We selected the tight frame introduced by Held *et al.* [36]. Finally, the filter design is reduced to [37]:

$$g(\lambda) = \begin{cases} cos\left(2\pi\,\mu\left(\frac{\lambda}{8\tau_1}\right)\right)) & if\ \tau_1 \le \lambda \le \tau_2 \\ sin\left(2\pi\,\mu\left(\frac{\lambda}{16\tau_1}\right)\right) & if\ \tau_2 \le \lambda \le \tau_3 \end{cases} \tag{18}$$

$$h(\lambda) = \begin{cases} 1 & if\ \lambda \le \tau_1 \\ sin\left(2\pi\,\mu\left(\frac{\lambda}{8\tau_1}\right)\right) & if\ \tau_1 \le \lambda \le \tau_2 \end{cases} \tag{19}$$

where $\mu(x) = -1 + 24x - 144x^2 + 256x^3$ and $\tau_1 = \frac{2}{3}$, $\tau_2 = 2\tau_1$, and $\tau_3 = 4\tau_1$. Scales of the wavelet can also be defined by: $t_j = 2^j\lambda_{max}^{-1}$ for $j = 0, \ldots, J-1$ where J is the number of scales. Selecting these values leads to a normal tight frame (frame boundaries equal to one). Figure 6 shows a comparison between conventional kernel values by Hammond *et al.* [18] and the Held kernels [36] used in this work. The scaling function $h(\lambda)$ is shown in blue, the wavelet functions $g(t_j\lambda)$ are in red, and $G(\lambda) = h(\lambda)^2 + \sum_{j=1}^{J} g(t_j\lambda)^2$ is shown in black. As it can be observed from the plot on the right, $G(\lambda)$ is constant (for desired range of λ) in the tight frame design, which leads to equal frame boundaries.

H. SUBSTITUTION OF THE PROPOSED WAVELET IN THE CONVENTIONAL BANDLET TRANSFORM

In final stage of this proposed algorithm, we devise a way to incorporate the proposed wavelet into the conventional Bandlet transform. To this end, we calculate the coefficients of the wavelet on graph and apply the "2D to 1D projection", "1D wavelet transform" and "thresholding on the 1D wavelet coefficients" in the given order. The main consideration in this stage is the thresholding method on the 1D wavelet values. We select the normal shrinkage method that provides the best results in our experiments [38], [39]. The value of the normal shrinkage threshold is obtained from:

$$T_N = \beta\hat{\sigma}_\upsilon^2/\hat{\sigma}_y \tag{20}$$

where $\hat{\sigma}_\upsilon$ is the calculated variance of noise, and $\hat{\sigma}_y$ is the standard deviation in desired sub-band:

$$\hat{\sigma}_y^2 = \frac{1}{M}\sum_{m=1}^{M} A_m^2 \tag{21}$$

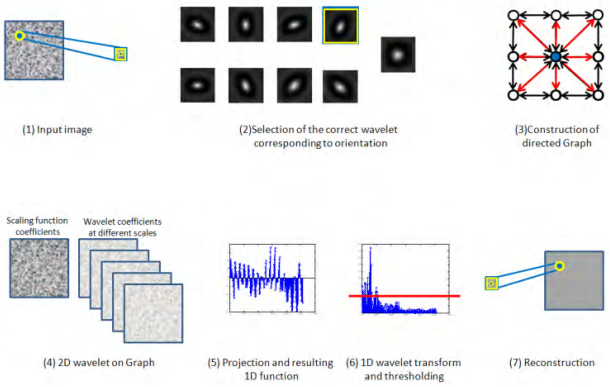

FIGURE 7. Demonstration of the BOG method "bandlet on an oriented graph".

where A_m stand for wavelet coefficients in selected sub-band and M is stands for entire number of wavelet coefficients in mentioned sub-band. The parameter β is given by:

$$\beta = \sqrt{\log\left(L_K/\mathrm{J}\right)} \tag{22}$$

where L_K is dimension of the subband in level K^{th}, and J is the decompositions' number.

We note that for calculation of $\hat{\sigma}_\upsilon$ as the noise variance, we assume that the 1D signal is a kind of shuffling on the 2D wavelet values, and the 1D wavelet transform retains the variance of the noise. Therefore, according to the characteristics of images in a given application, the noise variance can be estimated in the 2D wavelet on graph sub-bands, which is exemplified in the next section.

Figure 7 demonstrates the proposed BOG method in 7 steps, which are elaborated above in the whole section. Algorithm1 is the pseudo code for proposed Bandlet on Graph (BOG).

Algorithm 1 Bandlet on Graph

1: **Procedure** –BOG
2: **Input:** K patches extracted from the image by quadtree
3: **Output:** K denoised patches
4: **BEGIN**
5: Determine the orientation of each pixel by III-B (Figure 7-2)
6: Construct the directed graph (III-A)(Figure 7- 3)
7: Calculate the wavelet on graph (scaling image and wavelet images) (II-B with consideration of III- C and III-D)(Figure 7-4)
8: Project each of the wavelet images (Figure 7-5)
9: Apply 1D wavelet transform and thresholding according to III-E(Figure 7-6)
10: Reconstruct the patch (eq. (4) and more detail in [18]) (Figure 7-7)
11: **END**
12: **end procedure**

III. FIRST APPLICATION: DENOISING OF OPTICAL COHERENCE TOMOGRAPHY (OCT) IMAGES

In this section, we exemplify the presented bandlets on oriented graphs technique on an Optical Coherence Tomography (OCT) image denoising application. OCT is a method for crosswise imaging of objects using light beams [40]. In ophthalmologic applications, OCT found its place in early diagnosis of retinal diseases and layer-related abnormalities [41]. As a result of its similarity in image construction, OCT suffers from similar speckle noise that is observed in ultrasound images. It is important to consider that cohener waves in OCT produces speckle noise in axial and lateral paths. As a result,, the potent resolution in OCT data, reduces by this factor [42], [43]. It is also important to note that the mentioned speckle contains important textural information rather than virginal noise and this correlation should be considered in next calculations [44].

There is no doubt that noise reduction plays an important role in OCT image processing. It improves the visual inspection of the retinal layers for an ophthalmologist, and increases the performance of segmentation and registration algorithms [43], [45]. Denoising algorithms on OCT images can be categorized into 2 main classes: Complex domain methods and Magnitude domain methods [1], [43]. In complex domain methods, the noise management is done upon the optical setup and the methods are applied during the imaging procedure; however, in magnitude domain algorithms, a software-based method is applied offline on a previously-recorded scan.

In this research, we mainly focus on the second class of algorithms and compare the performance of 4 noise reduction algorithmsbased on: proposed bandlet on graph, 2D separable discrete wavelet transform, conventional bandlet, and 2D dual-tree complex wavelet transform [43].

A. METHOD OF FIRST APPLICATION

The methods are implemented in MATLAB version 7.9 (MathWorks, Natick, MA) with Image Processing Toolbox. We use a dataset from Topcon 3D OCT-1000 consisting of six 3-D OCTs, selected arbitrarily. The cases in this dataset are diagnosed with retinal Pigment Epithelial Detachment (PED) and all of them had given written informed consent. OCT images are acuired inFeiz Eye Center, Isfahan, Iran. The images are interpreted as 16 bit grayscale images ranging from 0 to 65,535. The tomograms are not log-compressed and the intensity was expressed in arbitrary units (AU) instead of decibels. The measurements are reported on seventy two arbitrarily selected slices.

The BOG method is a non-homomorphic technique and the transform is applied on multiplicative noise without using nonlinear operations like logarithm to change the multiplicative noise to additive noise. This idea is reported in [6]–[10] and the multiplicative model is proposed as:

$$x\left(i\right) = s\left(i\right) g(i) \tag{23}$$

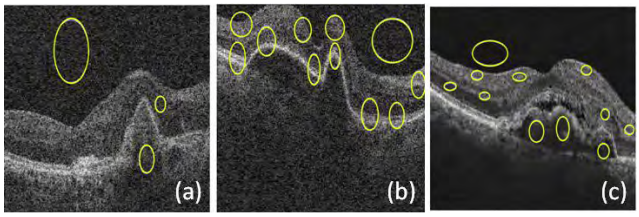

FIGURE 8. Samples of ROIs in finding a) CNR, b) EP, c) TP and ENL. The background ROIs are usually in bigger format, compared to foreground regions.

where i is the pixel index between 1 and whole pixel number, s is the pure signal, g is the speckle noise, and x is the observed data. After applying the transform directly on data, we have:

$$\begin{aligned} W\left(x\left(i\right)\right) &= W\left(s\left(i\right) g\left(i\right)\right) = W\left(s\left(i\right) + s\left(i\right)\left(g\left(i\right) - 1\right)\right) \\ W\left(x\left(i\right)\right) &= W\left(s\left(i\right)\right) + W\left(s\left(i\right)\left(g\left(i\right) - 1\right)\right). \end{aligned} \tag{24}$$

Hence we have an additive noise model in transform domain:

$$Y\left(k\right) = W\left(k\right) + N(k) \tag{25}$$

where $Y\left(k\right)$, $W\left(k\right)$, and $N(k)$ are respectively the k^{th} noisy transform coefficients, noise-free transform coefficients, and noise in the transform domain.

B. RESULTS OF FIRST APPLICATION ON REAL OCT DATA

CNR, Texture Preservation (TP), Edge Preservation (EP), and Equivalent Number of Looks (ENL) are the measured performance criteria, elaborated in [46]. The Regions of Interest (ROI) are demonstrated in Figure 8. The background ROIs are usually in bigger format, compared to foreground regions.

CNR represents the contrast between ROI and background. The TP shows how good is the method in retaining the original texture and ranges 0 and 1; One is expected original image without alternation. EP in ROI says how the algorithm takes care of the edges in original data, and ENL is a smoothness measure in homogenous regions

In this application, due to known structural property of the OCT images, the upper and lower regions of the image contain mainly the noise component in the signal. Accordingly, over a predefined window that is located in a lower area of the image in the 2D wavelet on graph sub-bands, we calculate the noise variance (Eq. 21), whose value is estimated as $\hat{\sigma}_y^2 = 15$.

The value of the performance measures for each denoising algorithm on seventy two arbitrarily selected slices is shown in Table 1. Figure 9 demonstrates samples of denoising with different methods.

As shown in Table 1, the performance of the BOG method surpasses the similar baseline method (the conventional bandlet). The results are slightly better than a recent methods [43], [44]

A small set of data is used for tuning the parameters to efficient and acceptable results. For instance, the images in this study have size of 512×650. The window size of 20×20 was selected empirically. Very small windows were not capable

TABLE 1. The performance measures for each denoising method in datasets from Topcon device.

	Original	Bandlet on Graph- BOG	2D separable DWT	Conventional bandlet	2D dictionary learning [43]	Gaussianization [44]
CNR	2.98±1.18	**30.11±7.03**	17.54±9.28	21.29±8.43	27.82±8.37	22.92±N/A
EP	1±0	0.89±0.10	0.81±0.04	0.85±0.07	0.87±0.02	**0.96±N/A**
TP	1±0	0.19±0.03	**0.25±0.05**	0.22±0.05	0.18±0.09	0.17±N/A
ENL	27.73±0.51	**2217.37±130.91**	669.21±107.53	1436.36±210.32	2183.26±229.51	N/A
time	--	3.49±0.96	**0.14±0.03**	2.23±0.61	5.25±0.42	83.22±N/A

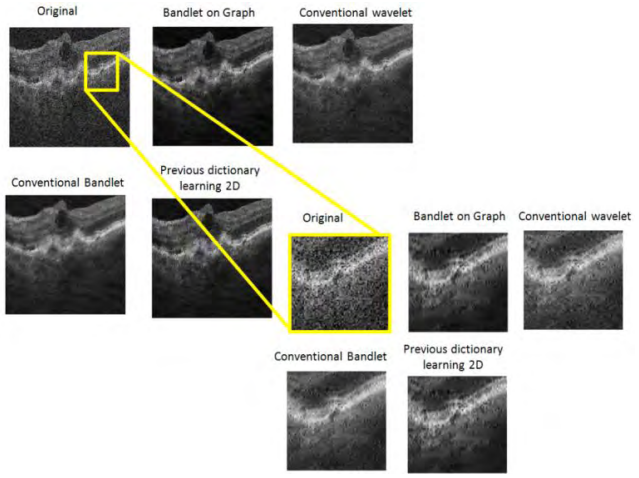

FIGURE 9. Samples of denoising with different methods.The right lower block shows the zoomed version for better comparison.

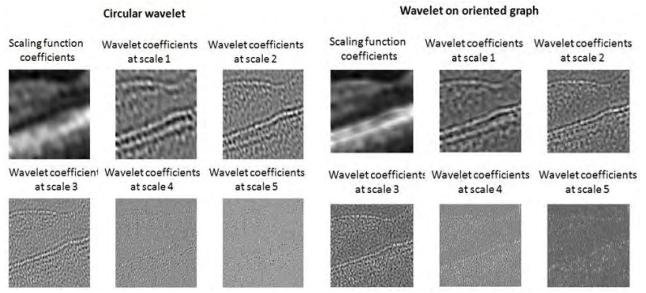

FIGURE 10. Comparison of the BOG method for construction of a directed graph (right block) with a circular wavelet ($\delta = 1$) (left block).

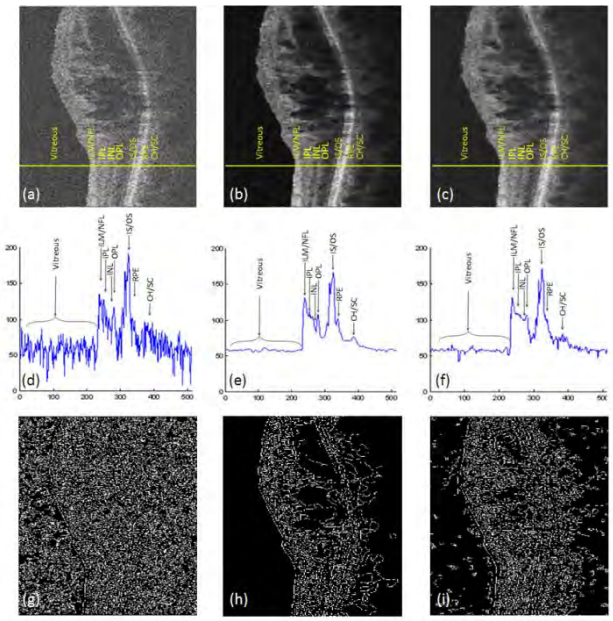

FIGURE 11. The cross-section 1D data along the yellow line. a) Original image taken from Topcon OCT device, b) the image after denoising with BOG method, c) image after denoising with conventional wavelet, d, e, f) corresponding cross section signals, g, h, i) Simple canny edge detector applied on a, b, c, respectively. ILM/NFL, inner limiting membrane/nerve fiber layer; IPL, inner plexiform layer; INL, inner nuclear layer; OPL, outer plexiform layer; ELM, external limiting membrane; IS/OS junction between the inner and outer segment of the photoreceptors; RPE, retinal pigment epithelium; CH/SC junction between the choroid and sclera.

of showing the orientation and big windows were suffering from multiple orientations in each area. This window size was also tested on images of size 256 × 256 and the results were acceptable. Regarding the orientations, the limited number 8 is selected since higher numbers would increase computation time; however, more orientation is expected to improve the results.

To provide a comparison between the BOG method for construction of a directed graph and a circular wavelet ($\delta = 1$), Figure 10 demonstrates a sample result. It can be noted that the resulting scaling function and wavelet coefficient are noticeably coarser and more blurred using the circular wavelet. The results become even worse if the 2D separable discrete wavelet transform were used; since the latter even suffers from a chalkboard artifact to the resulting images. This improvement can be justified by orientation-congruence of the BOG method.

As mentioned above, denoising is expected to facilitate the segmentation and registration process in OCT images. Many segmentation methods (with emphasis on A-scan or gradient-based methods) are very dependant on edge information [48]. The raw OCT image misses the weak edge features due to presence of speckle [49]. An ideal denoising method is expected to suppress the speckle noise and provide vivid edge features next segmentation steps. On the other hand, a weak denoising degrades the image features and makes segmentation worse. Figure 11 shows the performance of the proposed-BOG algorithm to suppress speckle noise and to produce identifiable peak and valley features. Furthermore, a simple edge detection on results of the BOG can demonstrate its feature preservation ability compared to the original image and that of a simple denoising method like conventional wavelet (Figure 11, g, h, i). Particularly, the effect of our

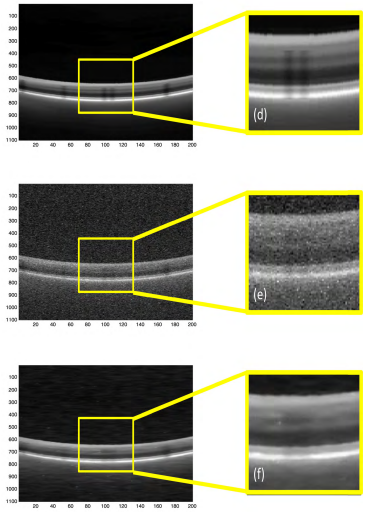

FIGURE 12. Evaluation of the BOG using synthetic OCT data. (a) Original noiseless synthesized OCT with synthesized vessels from [50], (b) Noisy version of (a) by method described in [51], (c) denoised image by BOG, (d-f) zoomed versions of (a-c).

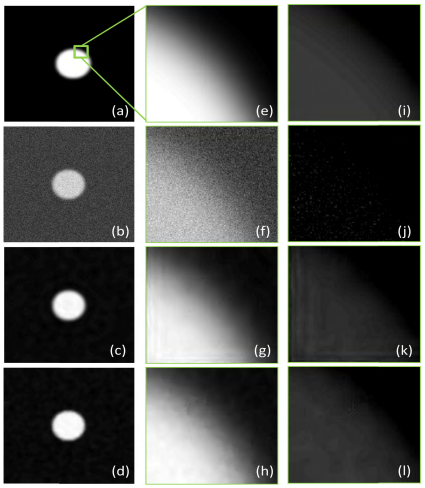

FIGURE 13. Comparison of tight frame steerable pyramid [7] and the BOG method. (a) original raw image, (b) Corrupted image by Gaussian noise with sigma = 20, (c) image after denoising with tight frame steerable pyramid [7], (d) denoised image by BOG. (e-f) cropped versions of (a-d), (i-l) reduced brightness for (e-h).

denoising method is visible in unveiling boundaries of layers like INL, RPE, Ch/Sc, thus facilitating a better segmentation phase following denoising.

C. RESULTS OF FIRST APPLICATION ON SYNTHETIC OCT DATA

The BOG is also validated using two hundred synthetic images from [50]. Noise was added with the method described in [51] using $\alpha_1 = 0.2$; $\alpha_2 = 0.2$; $\alpha_3 = 0.6$; $\beta_1 = 0.6$; $\beta_2 = 0.3$; $\beta_3 = 0.1$; $\sigma_1 = [1.5, 0.15]$; $\sigma_2 = [0.5, 0.5]$; block sizes of B1 = [2, 1]; B2 = [5, 1]; and a 100×100 patch of the vitreous in a real OCT. Mean PSNR value increased from 29.63 in original noisy images to 43.33 in the proposed method. One sample of the results is presented in Figure 12.

To compare the BOG with bare oriented wavelet transform, a comparison with [6] and [7] is presented. The oriented wavelet transform [6] is only based on two orientations (horizontal/ vertical or diagonal/anti-diagonal). Furthermore, the hidden Markov field (HMF) is used to model the orientation map, which is a time consuming process. The tight frame steerable pyramid in [7] is also a kind of oriented wavelet which is able to produce any possible orientation (similar to the proposed method). The local orientation is selected by maximizing the Hilbert transform of the original wavelet decompostion which does not lead to a high time complexity. However, the method is different from the BOG since an adapting algorithm is proposed in [7] which tailors the bases for each image by PCA. On the other hand, the proposed method has no training stage for execution.

The tight frame steerable pyramid [7] is compared to the BOG on a sample image provided by Jung [7] (Figure 13 (a-d)). The PSNR value is 41.86 for steerable pyramid method and 42.32 for the proposed method. The improvement is more obvious when the image is cropped to a smaller region (Figure 13 (e-h)) where the PSNR is 35.05 for steerable pyramid method and 42.79 for the BOG method. Figure 13 (i-l) show versions with reduced brightness of (e-h) to emphasize artifacts in (k).

IV. SECOND APPLICATION: DENOISING OF MICROSCOPIC IMAGES

The second application of the presented bandlets on oriented graphs technique is on photon-limited fluorescence microscopy images.

A. METHOD OF SECOND APPLICATION ON MICROSCOPIC IMAGES

Fluorescence microscopy is among methods which acquires the images by summing the number of photons and accordingly with very low signal-to-noise ratio [52]. The proposed method is tested on sample images provided by recent paper in this application [53]. The authors applied a noise modeled by combining Poisson and Gaussian probabilities. They also used the contourlet transform for representing the edges in produced data. The method was compared with state-of-the-art BM3D [53] method on two fluorescence microscopy data sets. The first data set is imaged with a Nikon C1 Plus confocal laser microscope (Medicinal Bioconvergence Research Center, Seoul National University). One hundred HeLa cells images are available in this data set, sized 512x512, and dye labeled in 3 fluorescent colors. The gold standard for calculation of measures like PSNR and SSIM is average of 100 images [53].

B. RESULTS OF SECOND APPLICATION ON HeLa CELLS IMAGES

Figure 14 and 15 demonstrates the results of BM3D, method by Yang and Lee [53], and the BOG method. The BOG shows capability of removing noise along with protection

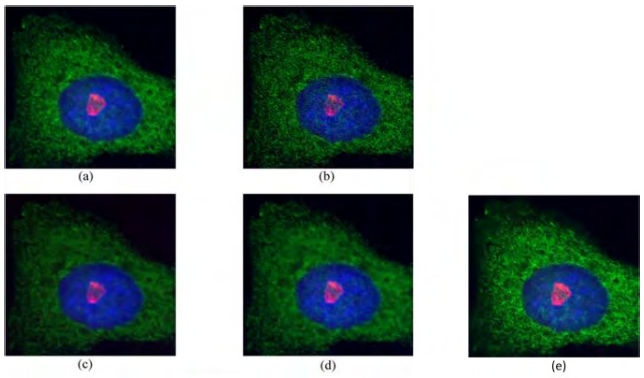

FIGURE 14. C (a) gold standard, (b) one sample image, (c) BM3D method, (d) the method introduced in [54], (e) the proposed method.

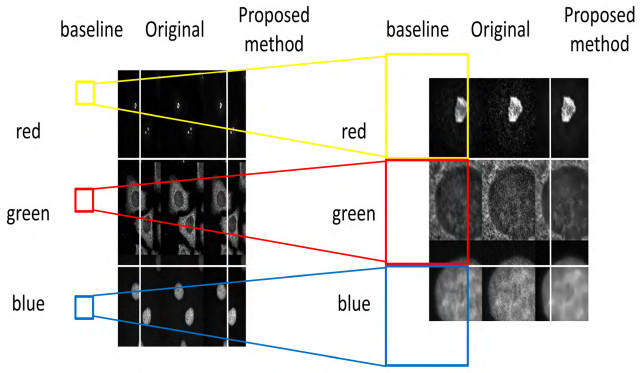

FIGURE 15. Comparison of proposed method with available methods for first dataset of HeLa cell images from [52] with emphasis on three channels. Left: different color channels along with baseline image, original input image, and results of denoising with BOG. Right: zoomed version of the left image.

TABLE 2. Comparison of PSNR(dB) between BOG method,BM3D and [54] each channel on the first dataset of HeLa cell images [54].

	channel R	channel G	channel B	Total
Raw image	28.64	21.95	28.41	26.33
BM3D with GAT	32.69	25.23	39.97	32.63
Method in [53]	35.58	29.53	36.94	34.02
Proposed BOG method	**36.12**	**30.47**	**39.14**	**35.24**

of the details in all three channels as elaborated in Figure 15. An average image computed from 100 images is used as the baseline image. The comparison of PSNR between BM3D, method in [54], and the BOG in each channel is presented in Table 2. The BOG method outperforms both of the mentioned methods in three channels.

The second image set were imaged with a Nikon A1R confocal laser (Department of Life Science, Ewha W. University). The data set has 40 HeLa cell images with size of 512x512, dye labeled in 2 fluorescentcolorsl. The gold standard is produced by averagingthe 40 [53]. To report the evaluation of denoising method in diverse noise levels, 3 datasets with different intensities were incorporated [53] but the related data is not released. Therefore, we compared our results with BM3D and method in [53] only on provided laser intensity of 0.4 in Figure 16. Furthermore, Figure 16 (e-g) shows local structural similarity (SSIM) value maps for mentioned methods to demonstrate the higher similarity

TABLE 3. Table III. Comparison of PSNR(dB) and SSIM between the BOG method with the BM3D and results of [53] with laser intensity equal to 0.4 (the second HeLa cell dataset [53]).

	PSNR(dB)	MSSIM
BM3D with modified Anscombe	23.21	0.7118
Method in [53]	23.44	0.8209
Proposed BOG method	**29.76**	**0.8928**

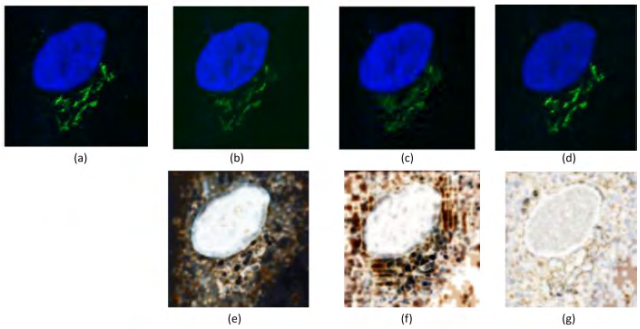

FIGURE 16. The second HeLa cell dataset [53] laser intensity equal to 0.4 (a) gold statndard, (b) BM3D, (c) the algorithm in [53], (d) the BOG method, (e, f, g) Local SSIM value map for (b, c, d), respectively.

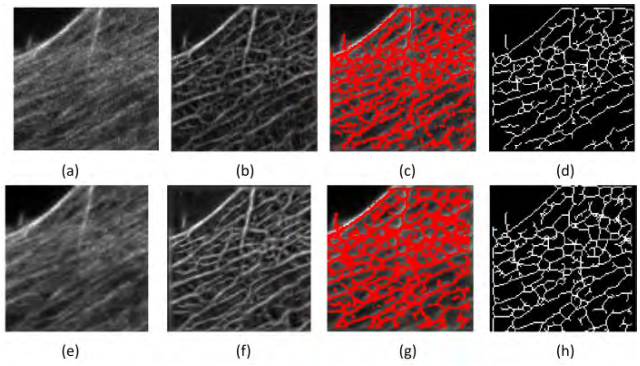

FIGURE 17. Filament extraction method. First row: results of [54] on original image, Second row: results of [53] on image after applying the BOG method. (a, e) The input image, (b, f) presence likelihood of a filament in each pixel, (c, g) centerlines of each likely filament, (d, h) the individual filaments.

of the proposed method to the original image. The PSNR results and mean structural similarity (MSSIM), provided in Table 3 show the numerical superiority of the BOG to other methods in this laser intensity.

C. RESULTS OF SECOND APPLICATION ON FILAMENT ENHANCEMENT

To show the ability of the BOG method as a pre-processing step for feature extraction in microscopic images, we concentrated on complete extraction and enumeration of individual filaments from the cellular cytoskeletal network as proposed by Basu *et al.* [54]. A new algorithm is proposed in [54] to find centerlines of filament bundles and to segment each filaments based on the identified centerlines.. A filament enhancement step is followed by localization method to find filaments automatically from microscopy images. We applied the proposed method on real confocal microscope images of

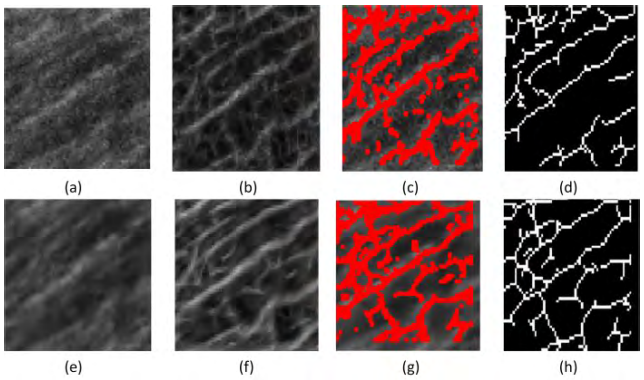

FIGURE 18. Filament extraction method (zoomed version of Fig. 17).

TABLE 4. Comparative table of the characteristics.

	Proposed BOG method
the original bandlet transform	the conventional wavelet is replaced by a new wavelet defined on a directed graph
conventional wavelet	The atoms of the new wavelet are tuned to be oriented according to the local edge characteristics in an image.
Non directed graph	due to the new construction on a directed graph, the edge weights on the graph take into account the local orientations directed from the current pixel towards its neighbors, rather than non-oriented edge weights.
Block based mathods with no overlap	the resulting image does not suffer from blocking artifacts. The reason is that the blocking is done on the 2D wavelet on graph and the inverse wavelet transform on graph filters out the artifact.
Algorithm which ignore the geometry	In each scale, the calculation of orientation and two stages of 2D and 1D wavelets are performed separately; therefore, the geometry of blocks remains unaffected and can be utilized in the reconstruction stage.
orthonormal transforms	Since the wavelet on graph is not orthogonal, the proposed bandlet on graph is not an orthonormal transform either.

flat cells (2D images) as provided by Basu *et al.* [54] and showed how the proposed method can improve the efficiency of [54]. Figure 17 and 18 show real examples demonstrating the extraction pipeline in [54]. The top row shows procedure in [54] on original data and the second row shows the results of [54] on data processed by the BOG method. The left column shows original images; the second column shown the presence likelihood of the filament in each pixel; The third column demonstrates the thresholded version of the previous image to provide a rough estimate of the filament place; The right panel shows the final resulrs of the algorithm in [54] too find each filament.

As can be observed in Figure 17 and particularly Figure 18, the filaments that were not visible in the output image on the right, are extracted after applying our BOG method. Visually, an increased sensitivity in the feature extraction step is obtained.

V. DISCUSSION AND CONCLUSIONS

The proposed BOG method takes advantage of both sparsity and multiscale characteristics of transform domain modeling, along with geometrical representation of graph based models. The properties of the proposed method is summarized in a comparative table of the characteristics.

According to the provided application on denoising of OCT images, it can be concluded that the proposed BOG method surpasses the similar 2D transforms in OCT image denoising. The method combines the properties of a conventional bandlet, with an orientation-adaptive strategy, which yields to better edge preservation and denoising. The performance is even slightly better than the 2D dictionary learning method with a complex wavelet start, which shows that the presented orientation tuning improves the performance of the method. The BOG method can be applied on a given stand-alone OCT image without requiring any training stage. Only required prior information about the image properties is an estimate on the noise variance, which is similar to any wavelet-based method that applies shrinkage. According to results on microscopic images, the BOG outperforms recent methods in denoising of Hella cells and filaments and can improve the feature extraction in such images.

The proposed method is theoretically expandable to 3D. Furthermore, the application of the proposed bandlet on oriented graphs to other image analysis tasks is an open future research direction.

ACKNOWLEDGEMENT

R. Kafieh and G. Unal were with the Faculty of Engineering and Natural Sciences, SabancıUniversity, 34965 Istanbul, Turkey. The authors would like to thank Alessio Montuoro for kindly providing 200 synthetic OCT data for evaluation. Also, they would like to thank Pedro Serranho for providing two samples of their synthesized OCTs.

For microscopic datasets, they would also like to thank S. Yang and B. U. Lee for sharing two online datasets for fixed HeLa cells and Gustavo Rohde for sharing online segmentation code and sample data.

REFERENCES

[1] Z. Amini and H. Rabbani, "Classification of medical image modeling methods: A review," *Current Med. Imag. Rev.*, vol. 12, no. 2, pp. 130–148, May 2016.
[2] E. J. Candès and D. L. Donoho, "Ridgelets: A key to higher-dimensional intermittency?" *Philos. Trans. Roy. Soc. London A, Math. Phys. Sci.*, vol. 357, no. 1760, pp. 2495–2509, Sep. 1999.
[3] S. AlZubi, N. Islam, and M. Abbod, "Multiresolution analysis using wavelet, ridgelet, and curvelet transforms for medical image segmentation," *Int. J. Biomed. Imag.*, vol. 2011, May 2011, Art. no. 136034.
[4] J.-L. Starck, E. J. Candes, and D. L. Donoho, "The curvelet transform for image denoising," *IEEE Trans. Electron. Packag. Manuf.*, vol. 11, no. 6, pp. 670–684, Jun. 2002.
[5] L. Dettori and L. Semler, "A comparison of wavelet, ridgelet, and curvelet-based texture classification algorithms in computed tomography," *Comput. Biol. Med.*, vol. 37, no. 4, pp. 486–498, Apr. 2007.
[6] M. N. Do and M. Vetterli, "The contourlet transform: An efficient directional multiresolution image representation," *IEEE Trans. Image Process.*, vol. 14, no. 12, pp. 2091–2106, Dec. 2005.
[7] A. Jung, "An introduction to a new data analysis tool: Independent component analysis," in *Proc. Workshop GK*," Regensburg, U.K.: Nonlinearity, Oct. 2001.
[8] I. Jolliffe, *Principal Component Analysis*. Hoboken, NJ, USA: Wiley, 2002.
[9] I. Tosic and P. Frossard, "Dictionary learning," *IEEE Signal Process. Mag.*, vol. 28, no. 2, pp. 27–38, Mar. 2011.

[10] Y. Wiaux, J. D. McEwen, P. Vandergheynst, and O. Blanc, "Exact reconstruction with directional wavelets on the sphere," *Monthly Notices Roy. Astronomical Soc.*, vol. 388, no. 2, pp. 770–788, Jul. 2008.
[11] J.-P. Antoine, I. Bogdanova, and P. Vandergheynst, "The continuous wavelet transform on conic sections," *Int. J. Wavelets, Multiresolution Inf. Process.*, vol. 6, pp. 137–156, Mar. 2008.
[12] B. Peng, L. Zhang, and D. Zhang, "A survey of graph theoretical approaches to image segmentation," *Pattern Recognit.*, vol. 46, no. 3, pp. 1020–1038, Mar. 2013.
[13] A. Shokoufandeh and S. Dickinson, "Graph-theoretical methods in computer vision," in *Theoretical Aspects of Computer Science* (Lecture Notes in Computer Science), vol. 2292. 2002, pp. 148–174.
[14] M. Crovella and E. Kolaczyk, "Graph wavelets for spatial traffic analysis," in *Proc. 22nd Annu. Joint Conf. IEEE Comput. Commun. Societies*, Mar./Apr. 2003, pp. 1848–1857.
[15] A. Smalter, J. Huan, and G. Lushington, "Graph wavelet alignment kernels for drug virtual screening," *J. Bioinf. Comput. Biol.*, vol. 7, pp. 473–497, Jun. 2009.
[16] R. R. Coifman and M. Maggioni, "Diffusion wavelets," *Appl. Comput. Harmon. Anal.*, vol. 21, no. 1, pp. 53–94, 2006.
[17] D. Geller and A. Mayeli, "Continuous wavelets on compact manifolds," *Mathematische Zeitschrift*, vol. 262, pp. 895–927, Aug. 2009.
[18] D. K. Hammond, P. Vandergheynst, and R. Gribonval, "Wavelets on graphs via spectral graph theory," *Appl. Comput. Harmon. Anal.*, vol. 30, no. 2, pp. 129–150, Mar. 2011.
[19] D. Thanou, D. I. Shuman, and P. Frossard, "Parametric dictionary learning for graph signals," in *Proc. IEEE Global Conf. Signal Inf. Process. (GlobalSIP)*, Dec. 2013, pp. 487–490.
[20] S. Mallat, *A Wavelet Tour of Signal Processing*. New York, NY, USA: Academic, 1999.
[21] P. J. Burt and E. H. Adelson, "The Laplacian pyramid as a compact image code," *IEEE Trans. Commun.*, vol. COM-31, no. 4, pp. 532–540, Apr. 1983.
[22] N. Kingsbury, "Complex wavelets for shift invariant analysis and filtering of signals," *Appl. Comput. Harmon. Anal.*, vol. 10, no. 3, pp. 234–253, May 2001.
[23] E. J. Candès and D. L. Donoho, "New tight frames of curvelets and optimal representations of objects with piecewise C2 singularities," *Commun. Pure Appl. Math.*, vol. 57, no. 2, pp. 219–266, Feb. 2004.
[24] E. L. Pennec and S. Mallat, "Sparse geometric image representations with bandelets," *IEEE Trans. Image Process.*, vol. 14, no. 4, pp. 423–438, Apr. 2005.
[25] G. Peyré, E. Le Pennec, C. Dossal, and S. Mallat, "Geometrical image estimation with orthogonal bandlet bases," *Proc. SPIE*, vol. 6701, Sep. 2007, pp. 67010M.1–67010M.10.
[26] G. Peyré and S. Mallat, "A matlab tour of second generation bandelets," *CMAP, Ecole Polytechnique*, vol. 395, pp. 1–7, 2005.
[27] G. Peyré and S. Mallat, "Surface compression with geometric bandelets," *ACM Trans. Graph.*, vol. 24, no. 3, pp. 601–608, Jul. 2005.
[28] R. R. Coifman and D. L. Donoho, "Translation-invariant de-noising," in *Wavelets Statistics* (Lecture Notes in Statistics), vol. 103. 1995, pp. 125–150.
[29] J. Portilla, V. Strela, M. J. Wainwright, and E. P. Simoncelli, "Image denoising using scale mixtures of Gaussians in the wavelet domain," *IEEE Trans. Image Process.*, vol. 12, no. 11, pp. 1338–1351, Nov. 2003.
[30] W. T. Freeman and E. H. Adelson, "The design and use of steerable filters," *IEEE Trans. Pattern Anal. Mach. Intell.*, vol. 13, no. 9, pp. 891–906, Sep. 1991.
[31] D. K. Hammond, L. Jacques, and P. Vandergheynst, "Image modeling with nonlocal spectral graph wavelets," in *Image Processing and Analysis with Graphs: Theory and Practice*, O. Lezoray and L. Grady, Eds. Boca Raton, FL, USA: CRC Press, 2011.
[32] W. H. Press, B. P. Flannery, S. A. Teukolsky, and W. T. Vetterling, *Numerical Recipes in Fortran 77: The Art of Scientific Computing*. New York, NY, USA: Cambridge Univ. Press, 1992, p. 933.
[33] D. S. Watkins, *Fundamentals of Matrix Computations*, vol. 64. Hoboken, NJ, USA: Wiley, 2004.
[34] P. Per-Olof, "Lecture 16 the QR algorithm," Massachusetts Inst. Technol., Cambridge, MA, USA, Tech. Rep. MIT 18.335J/6.337J, 2006.
[35] J. Kovačević and C. Amina, "An introduction to frames," *Found. Trends Signal Process.*, vol. 2, no. 1, pp. 1–94, 2008.
[36] S. Held, M. Storath, P. Massopust, and B. Forster, "Steerable wavelet frames based on the riesz transform," *IEEE Trans. Image Process.*, vol. 19, no. 3, pp. 653–667, Mar. 2010.
[37] N. Leonardi and D. Van De Ville, "Tight wavelet frames on multislice graphs," *IEEE Trans. Signal Process.*, vol. 61, no. 13, pp. 3357–3367, Jul. 2013.
[38] R. Sihag, R. Sharma, and V. Setia, "Wavelet thresholding for image denoising," in *Proc. Int. Conf. VLSI, Commun. Instrum.*, 2011, pp. 21–24.
[39] S. Sutha, E. J. Leavline, and D. A. A. G. Singh, "A comprehensive study on wavelet based shrinkage methods for denoising natural images," *WSEAS Trans. Signal Process.*, vol. 9, no. 4, pp. 203–215, Oct. 2013.
[40] D. Huang *et al.*, "Optical coherence tomography," *Science*, vol. 254, no. 5035, pp. 1178–1181, 1991.
[41] M. R. Hee *et al.*, "Optical coherence tomography of the human retina," *Arch. Ophthalmology*, vol. 113, no. 3, pp. 325–332, Mar. 1995.
[42] M. Szkulmowski, I. Gorczynska, D. Szlag, M. Sylwestrzak, A. Kowalczyk, and M. Wojtkowski, "Efficient reduction of speckle noise in optical coherence tomography," *Opt. Express*, vol. 20, no. 2, pp. 1337–1359, 2012.
[43] R. Kafieh, H. Rabbani, and I. Selesnick, "Three dimensional data-driven multi scale atomic representation of optical coherence tomography," *IEEE Trans. Med. Imag.*, vol. 34, no. 5, pp. 1042–1062, May 2015.
[44] Z. Amini and H. Rabbani, "Optical coherence tomography image denoising using Gaussianization transform," *J. Biomed. Opt.*, vol. 22, no. 8, Aug. 2017, Art. no. 086011.
[45] N. M. Grzywacz *et al.*, "Statistics of optical coherence tomography data from human retina," *IEEE Trans. Med. Imag.*, vol. 29, no. 6, pp. 1224–1237, Jun. 2010.
[46] H. Rabbani, M. Sonka, and M. D. Abramoff, "Optical coherence tomography noise reduction using anisotropic local bivariate," *J. Biomed. Imag.*, vol. 2013, Jan. 2013, Art. no. 22.
[47] A. Pizurica *et al.*, "Multiresolution denoising for optical coherence tomography: A review and evaluation," *Current Med. Imag.*, vol. 4, pp. 270–284, Nov. 2008.
[48] R. Kafieh, H. Rabbani, M. D. Abramoff, and M. Sonka, "Intra-retinal layer segmentation of 3D optical coherence tomography using coarse grained diffusion map," *Med. Image Anal.*, vol. 17, no. 8, pp. 907–928, Dec. 2013.
[49] F. Luan and Y. Wu, "Application of RPCA in optical coherence tomography for speckle noise reduction," *Laser Phys. Lett.*, vol. 10, no. 3, pp. 35–43, 2013.
[50] A. Montuoro, S. M. Waldstein, B. Gerendas, G. Langs, C. Simader, and U. Schmidt-Erfurth, "Statistical retinal OCT appearance models," *Investigative Ophthalmology Vis. Sci.*, vol. 55, p. 4808, Apr. 2014.
[51] P. Serranho, C. Maduro, T. Santos, J. Cunha-Vaz, and R. Bernardes, "Synthetic OCT data for image processing performance testing," in *Proc. 18th IEEE Int. Conf. Image Process.*, Sep. 2011, pp. 401–404.
[52] F. Luisier, T. Blu, and M. Unser, "Image denoising in mixed Poisson–Gaussian noise," *IEEE Trans. Image Process.*, vol. 20, no. 3, pp. 696–708, Mar. 2011.
[53] S. Yang and B. U. Lee, "Poisson-Gaussian noise reduction using the hidden Markov model in contourlet domain for fluorescence microscopy images," *PLoS ONE*, vol. 10, Sep. 2015, Art. no. e0136964.
[54] S. Basu, C. Liu, and G. K. Rohde, "Extraction of individual filaments from 2D confocal microscopy images of flat cells," *IEEE/ACM Trans. Comput. Biol. Bioinformatics*, vol. 12, no. 3, pp. 632–643, May 2015.

RAHELE KAFIEH received the B.S. degree from the Sahand University of Technology, Iran, in 2005, and the M.Sc. and Ph.D. degrees in biomedical engineering from the Isfahan University of Medical Sciences, Isfahan, Iran, in 2008 and 2014, respectively. This work was conducted (partially) in SabancıUniversity, Istanbul, Turkey, when she was a Visiting Postdoctoral Fellow with the Faculty of Engineering and Natural Sciences, SabancıUniversity (in 2015 and awarded by the TUBITAK 2216 Scholarship). She is currently an Assistant Professor with the School of Advanced Technologies in Medicine, Isfahan University of Medical Sciences, and also a Guest Researcher with the NeuroCure Clinical Research Center, Charite University, Berlin, Germany, awarded by the EINSTEIN Forum. She is also a Section Editor of biomedical image processing in the *Journal of Medical Signal and Sensors* (JMSS).

HOSSEIN RABBANI received the B.Sc. degree (Hons.) in electrical engineering (communications) from the Isfahan University of Technology and the M.Sc. degree and the Ph.D. degree in biomedical engineering (bioelectrics) from the Amirkabir University of Technology (Tehran Polytechnic). He was a Visiting Research Scholar with Queen's University. He was also a Postdoctoral Research Fellow with Duke University and a Postdoctoral Research Scholar with The University of Iowa. He is currently a Professor with the Medical Image and Signal Processing Research Center, Biomedical Engineering Department, Isfahan University of Medical Sciences. His research topics include medical image analysis and modeling, statistical (multidimensional) signal processing, sparse transforms, and image/video restoration. He is also the Chief Editor of the *Journal of Medical Signal and Sensors* (JMSS).

GOZDE UNAL received the Ph.D. degree in electronics and communication engineering, with a minor in mathematics, from North Carolina State University, NC, USA, in 2002. She was a Postdoctoral Fellow with the Georgia Institute of Technology, USA. Between 2003 and 2007, she was a Research Scientist with Siemens Corporate Research, Princeton, NJ, USA. Between 2007 and 2015, she was an Assistant Professor and an Associate Professor with the Faculty of Engineering and Natural Sciences, SabancıUniversity. In 2015, she joined the Department of Computer Engineering, Istanbul Technical University, where she is currently a Full Professor. Her research interests include computer vision and machine learning. She was the recipient of the L'Oreal Turkey's Female Scientist Award in Life Sciences, in 2010. She received the Marie Curie Alumni Association (MCAA) Career Award from the European Commission, in 2017. She served as a Technical Program Co-Chair for the MICCAI 2016. She is a Technical Program Co-Chair of the Medical Imaging with Deep Learning (MIDL) Conference 2019.